7

Computational Flowfield Analysis of a Planetary Entry Vehicle

Antonio Viviani[1] and Giuseppe Pezzella[2]
[1]*Seconda Università degli Studi di Napoli, via Roma 29, 81031 Aversa,*
[2]*Centro Italiano Ricerche Aerospaziali, via Maiorise, 81043 Capua*
Italy

1. Introduction

Computational Fluid Dynamics (CFD) analysis represents a key technology within planetary entry vehicle design. Safe landing of vehicles re-entering from space requires, in fact, an accurate understanding of all physical phenomena that take place in the flowfield past the hypersonic vehicle to assess its aerodynamics and aerothermodynamics performance. CFD allows to significantly reduce the number of in-flight and plasma wind-tunnel (PWT) experimental test campaigns and to account for real-gas flow features, which are difficult to reproduce in ground-test facilities. Flight measurements collected during re-entry have demonstrated that real gas effects strongly influence both aerodynamics and aerothermal loads of hypervelocity vehicles. On the other hand, trajectory calculation for atmospheric re-entry involves determination of vehicle aerodynamics and aerothermodynamics. As a consequence, accurate modeling of flow physics, in particular flow chemistry is fundamental to reliably design re-entry vehicles.
In this chapter, we stress this point with an application to a capsule-type crew return vehicle (CRV) for the International Space Station (ISS) support servicing.
However, high accuracy in modeling flow and chemistry coupling may produce only a small increase in the numerical results accuracy, despite the high modeling efforts and the increased computational cost. So, one must balance the theoretical and computer time effort needed to use a more general and sophisticated model against the expected accuracy of results. The question then arises as to what extent the number of reactions, coefficients, reaction mechanism, etc. influence the flow. To answer this question, a step-by-step numerical investigation has been carried out to examine the influence of the chemical reactions, its mechanisms and kinetics, and of thermal non-equilibrium on the air flows past the CRV, in the framework of a low Earth orbit (LEO) scenario. Two-dimensional axi-symmetric and three-dimensional Navier-Stokes computations are performed, for perfect gas and reacting gas mixture in thermal and chemical non-equilibrium, and for several chemical reaction mechanisms. In particular, simulations are computed with different wall-surface boundary conditions: non-catalytic wall (NCW), partially catalytic wall (PCW), fully catalytic wall (FCW) to underline the effect of the heat shield catalyticity on the vehicle aerodynamic heating. The work confirms that high-temperature transport phenomena markedly influence the vehicle flowfield and, in turn, the vehicle aerodynamics and aerothermodynamics, but it also stresses that, with an acceptable loss of results accuracy, we

do not need to use models of such high complexity, and therefore considerable computing time can be saved.

2. Real gas effects and re-entry hypersonic flight

During atmospheric descent, re-entry vehicles encounter several flow regimes and thermochemical phenomena: they fly from free molecular to fully continuum phases and, when in continuum, from laminar to fully turbulent flows. When freestream enthalpy is large enough the flow passing through the bow shock dissociates resulting in a several species reacting mixture flow around the vehicle. The thermal and chemical characteristics of the gas in the shock layer are altered depending on the atomic and molecular structure of the air species (Sarma, 1995). For instance, when flow velocity is low, energy is absorbed only into particles vibration and rotation degrees of freedom (dof). But as velocity sufficiently increases, the thermal energy of the gas becomes comparable with the energy associated with a whole range of gas phase chemical processes, such as the excitation of molecular modes of vibration; the dissociation of oxygen and nitrogen; the formation of other chemical species through recombination reactions; the ionisation of both molecular and atomic species.

As a consequence, the flowfield chemical composition around the re-entry vehicle varies spatially and temporally and, because shock layer molecules continuously exchange their energy between the translational and internal dof, the air can result in a thermal-and/or chemical non-equilibrium mixture. Then, the microscopic structure of the mixture species, affecting the ways in which energy may be redistributed, influences the specific heat ratio (γ), the chemical reaction rates, and the transport properties. These quantities, in turn, affect the dynamics of the flow as well as shock and expansion waves (i.e. pressure, temperature, and velocity distributions), the chemical energy diffused to the surface (i.e. the chemical contribution to the heat flux at the wall), the boundary layer structure (i.e. the heat flux and shear stress). In particular, the flow chemical dissociation results in a large density ratio (ε) across the strong bow shock, which markedly influences the capsule's aerodynamics. In fact, ε influences the shock shape, the stand-off distance, and the wall-surface pressure that, at the stagnation point (e.g., Cp_{max}), reads:

$$C_{p\max} = C_{pt2} = \frac{P_{t2} - P_\infty}{q_\infty} = \left(\frac{P_{t2}}{P_\infty} - 1\right)\frac{2}{\gamma M_\infty^2} \cong 2 - \varepsilon \tag{1}$$

where ε, in the hypersonic limit, is:

$$\varepsilon = \lim_{M_\infty \to \infty} \frac{\rho_1}{\rho_2} = \frac{\gamma - 1}{\gamma + 1} \tag{2}$$

High temperature effects also modify the hypersonic capsule-vehicle aerodynamics and aerothermodynamics by means of a very abrupt change in the CRV trim angle of attack (α_{trim}). This is due to the shift of the sonic line position at the vehicle leeside because of the change in γ, thus affecting the CRV pitching moment (CM_Y) (Hassan et al., 1993) and, hence, the capsule static stability that is a critical requirement for a re-entry vehicle, because static instability could lead to catastrophic failure if the thermal shield is not protecting the vehicle anymore. Real gas effects also influence vehicle aeroheating since thermal protection material (TPM) could promote the chemical recombination at wall of flowfield atomic

species thus increasing the overall heat flux up to two times or more than the value of a non-catalytic wall (Scott, 1997). For instance, the reactions considered above, taking place only in the gas phase, are termed as homogeneous chemical reactions and differ from the heterogeneous ones that, instead, occur near the vehicle wall involving gas and solid species. They can be catalyzed by the TPM and, being exothermic, contribute to the vehicle aeroheating. Thus, the TPM, promoting or preventing species recombination at wall, depending on its catalyticity, plays an important role in the aerodynamic heating. Neglecting conduction into the heatshield and radiation from the gas, the energy balance at the vehicle surface reads:

$$-\dot{q}_r = -\sigma\,\varepsilon\,T_w^4 = \lambda_{tr}\left(\frac{\partial T}{\partial n}\right)_w + \sum_{i=1}^{N_v}\lambda_{v,i}\left(\frac{\partial T_{v,i}}{\partial n}\right)_w + \rho\sum_{i=1}^{N_s}\left(\int_{T_o}^{T} C_{Pi}\,dT + \Delta h_{fi}^{o}\right) D_i\left(\frac{\partial Y_i}{\partial n}\right)_w \qquad (3)$$

The first term, on the right-hand side, is the conductive heat-flux, the second one is the vibrational contribution, and the last one is the species diffusion contribution that strongly depends on the catalytic properties of thermal protection system (TPS). Therefore, the heatshield should be a poor catalyst (Anderson, 1973).

Of course the entire above mentioned scenario depends on the kind of re-entry (i.e. orbital or superorbital one). For example, flowfield computation involving ionized species, as for superorbital reentries, requires at least 11 chemical species with 20 reactions, whereas for lower velocity reentries, 5 non-ionized species and 17 reactions are sufficient (Sarma, 1995). Therefore, a reliable numerical simulation of re-entry flows can be very challenging, depending on the more or less correct and accurate modelling of the flowfield thermo-chemical processes. In this framework simulation problems may arise as the coupling of flow and chemistry leads to a stiff problem due to differences in reaction rate characteristic times (Anderson, 1989); dissociation rate coefficients can differ by orders of magnitude and, since reaction rates are very difficult to measure, different values may exist for the same coefficient. As a result, the appropriate set of reactions to be used represents a very relevant choice, especially if one considers that, in general, an increased model complexity does not entail a greater accuracy of numerical results, despite the higher computational cost needed for increased reactions set. Moreover, when one increases the number of chemical reactions, numerical results can be more influenced by the effect of the uncertainty in input data, such as species transport coefficients, relaxation times for thermal and chemical non-equilibrium. So, it could be important to simplify the reaction mechanisms, by reducing as much as possible the number of chemical reactions, without loss in accuracy but greatly reducing computing time.

3. CRV concept and re-entry flight scenario

The re-entry system is an Apollo-like capsule measuring about 5 m in diameter (D), with a nose radius (R_N) of 6.05 m; the sidewall angle (θ) of 33 deg and the overall vehicle height of 3.8 m (see Fig. 1). The offset centre of gravity (cg) is located at x/D=0.26 and y/D=-0.0353.

This vehicle concept represents a scaled-up version of the ARD capsule, which is a flying test bed successfully experimented by ESA in October 1998 (Walpot, 2001).

The reference mission scenario considered for the CRV is the re-entry from the ISS orbit performed by a vehicle weighting about 9 ton, starting from the atmospheric entry interface (h_E=120 km) with V_E=8 km/s inertial, and θ_E=-2 deg. The re-entry flight scenario is given in

both altitude-velocity map and Mach-Reynolds plane in Fig. 2. These re-entry trajectories have been computed by means of the ENTRY (ENtry TRajectrY) code developed at SUN (Viviani, 2006). The blue curve is a ballistic descent trajectory, while the red one refers to a lifting return since the capsule, flying trimmed at α=20 deg constant over the critical heating regime, is employing aerodynamic lift to sustain the descent flight path. As shown, the capsule, moving from a very rarefied atmosphere to a denser one, shifts from the free molecular flow (FMF) regime, where $Kn_\infty \geq 10$ and individual molecular collisions are important, to the transition one, where $10^{-3} < Kn_\infty < 10$ and slip effects are important, and then to the continuum regime where $Kn_\infty \leq 10^{-3}$. For instance, the similarity parameter that governs these different flow regimes is the Knudsen number (Bertin, 1994):

$$Kn_{\infty L_{ref}} = \frac{\lambda}{L_{ref}} = 1.25\sqrt{\lambda}\,\frac{M_\infty}{Re_{\infty L_{ref}}} \tag{4}$$

where L_{ref} is the characteristic length of the body (e.g., the capsule diameter). Therefore, vehicle aerodynamics must also consider the effect of the Kundsen number. Re-entry trajectories of Fig.2 result in an aerothermal environment that must be accurately predicted for a reliable TPS design (Pezzella et al., 2007). To this end, trajectory freestream flight conditions have been used to perform numerical computations, as reported hereinafter.

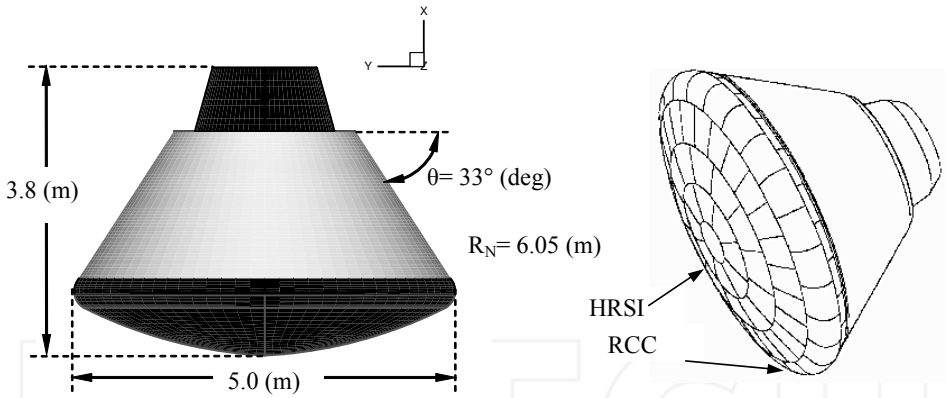

Fig. 1. CRV Vehicle configuration with quotes and TPS layout with high reusable surface insulator (HIRS) and reinforced carbon-carbon (RCC) tiles

4. Design approaches and numerical tools

The preliminary AErodynamic DataBase (AEDB) of the CRV has been provided according to the space-based design approach (Prabhu, 2004), which dictates the generation of data set as function of a number of independent parameters (i.e. M_∞, Re_∞, α, β).

On the other hand, the preliminary AeroThermodynamic DataBase (ATDB) has been computed following the trajectory-based design approach, which consists in performing aerothermal computations at a finite number of "critical" points of the nominal re-entry trajectory (Olynick, 1998).

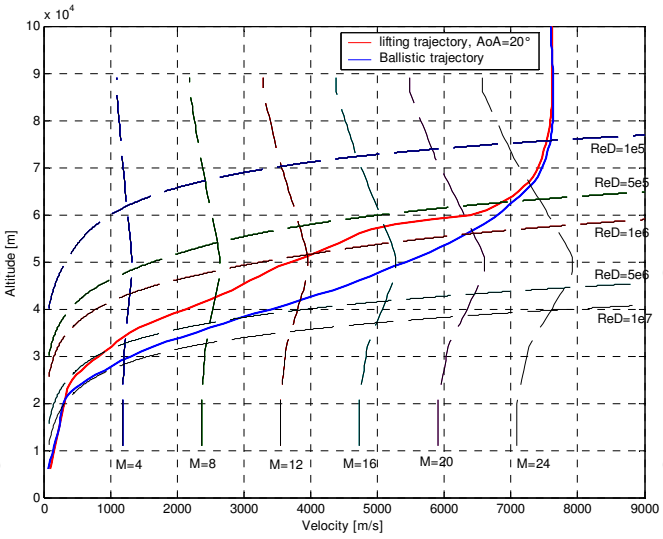

a)

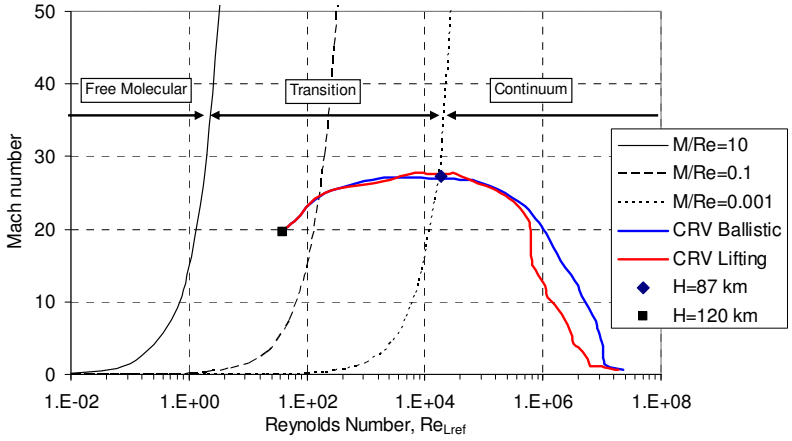

b)

Fig. 2. Re-entry flight scenario; a) altitude-velocity map; b) Mach-Reynolds map with constant Knudsen numbers

Computational analysis of the CRV flowfield is performed by means of the solver code Fluent together with several user defined functions (UDF), developed by the authors, in order to manage vibrational relaxation, several catalyticity models, radiative equilibrium at the wall and other boundary conditions. Computations have been carried out on multiblock structured grids. A close-up view of both 2-D and 3-D mesh can be seen in Fig. 3. The grid used for 3D calculations consists of 32 blocks with about 900.000 cells. For each computational case, a new grid has been created to properly accommodate for the detached bow shock location. See (Viviani et al., 2008) for further details on the computational grids.

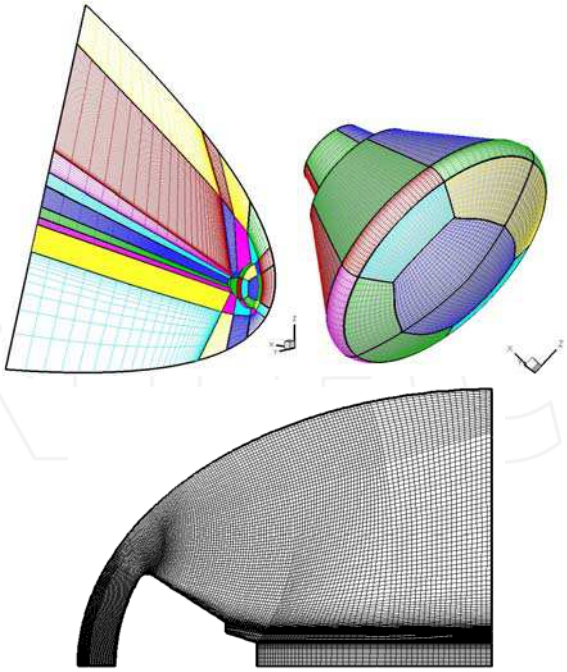

Fig. 3. Close-up view of 3-D (on top) and 2-D axi-symmetric computational mesh domains

5. The model and the numerical technique

The mathematical model describing the flowfield around a hypervelocity vehicle deals with balance equations for a multi-species chemically reacting gas mixture supplemented with an appropriate set of chemical reactions (i.e. the reactions mechanism) and with equations modelling species vibrations relaxation (i.e. thermal non-equilibrium).

5.1 Flowfield governing equations

The governing equations are made up of equations for mass conservation, total momentum balance, total energy (without the vibrational one) conservation, individual species balance and vibrational energy conservation. The full set of equations for a laminar viscous compressible continuum flow in thermal and chemical non-equilibrium, assuming the air as a mixture of N_S perfect gases and N_v vibrating species, written in the integral conservation is (Gnoffo et al., 1989):

$$\frac{\partial}{\partial t}\int_V \vec{W}\,d\upsilon + \int_S \left(\vec{F}_{inv} + \vec{F}_{vis}\right)\cdot\vec{n}\,dS + \frac{\Gamma}{r}\int_V \left(\vec{A}^*_{inv} + \vec{A}^*_{vis}\right)dV = \int_V \vec{\Omega}\,dV \tag{5}$$

where $\vec{W} = \left[\rho, \rho u, \rho v, \rho w, e_t, \rho_1, ..., \rho_{Ns-1}, \rho e_{v1}, ..., \rho e_{vN_v}\right]$ is the unknown state vector of the conserved quantities, in which ρ is the fluid density, ρu, ρv and ρw are the momentum densities, e_t is the total internal energy per unit mass, ρ_i and e_{vi} are, respectively, the density and the vibrational energy of the i^{th} species while ρe_{vi} takes into account for vibrational

energy conservation. $\vec{F}$ and $\vec{A}^*$, splitted into an inviscid and a viscous part, are the flux vector and the axis-symmetric terms matrixes, respectively. Γ is equal to 1 for axis-symmetric flows and 0 for 2D and 3D flows. $\vec{\Omega} = \left[0,0,0,0,0,\Omega_1,.....,\Omega_{Ns-1},\Omega_{v1},.....,\Omega_{vN_v}\right]^T$ is the source terms vector. It defines the mass and energy exchange among the species as a result of the chemical reaction rate and the energy transfer due to the internal energy excitation processes (Bertin, 1994). Finally, V is the arbitrary control volume cell, S is its closed boundary control surface and $\vec{n}$ is the outward normal unit vector (Anderson, 1989).
Eq.(5) can be written in differential form as follows:
Continuity:

$$\frac{\partial \rho}{\partial t} + \vec{\nabla} \cdot \left(\rho \vec{V} \right) = 0 \tag{6}$$

Momentum:

$$\frac{\partial \left(\rho \vec{V} \right)}{\partial t} + \vec{\nabla} \cdot \left(\rho \vec{V} \vec{V} \right) + \vec{\nabla} p = 2\vec{\nabla} \cdot \left[\mu \left(\vec{\nabla} \vec{V} \right)_o^s \right] \tag{7}$$

Energy:

$$\frac{\partial \left(\rho e_t \right)}{\partial t} + \vec{\nabla} \cdot \left[\left(\rho e_t + p \right) \vec{V} \right] = \vec{\nabla} \cdot \left[\lambda \nabla T + 2\mu \left(\vec{\nabla} \vec{V} \right)_o^s \cdot \vec{V} + \sum_i h_i \vec{J}_i \right] - \sum_i h_i \dot{\omega}_i - \sum_j \dot{e}_{vj} \tag{8}$$

Species:

$$\frac{\partial \left(\rho Y_i \right)}{\partial t} + \vec{\nabla} \cdot \left(\rho \vec{V} Y_i \right) + \vec{\nabla} \cdot \vec{J}_i = \dot{\omega}_i \tag{9}$$

Vibrational energy:

$$\frac{\partial \left(\rho e_{vj} \right)}{\partial t} + \vec{\nabla} \cdot \left(\rho \vec{V} e_{vj} \right) = \dot{e}_{vj} \tag{10}$$

In these equations, $\vec{V}$ is the velocity vector, Y_i is the mass fraction of the i^{th} species and, $\dot{\omega}_i$ is the rate of change of ρ_i due to chemical reactions, J_i is the diffusive flux of i^{th} species, which arises due to concentration gradients, M_i and h_i are, respectively, the molecular weight and enthalpy of i^{th} species, p is the pressure, μ is the viscosity and λ is the thermal conductivity. For each species the perfect gas model applies and the Dalton's law holds:

$$p = \sum_i p_i \tag{11}$$

where p_i is the partial pressure of the i^{th} species of the mixture. As a consequence, the following relation for density reads:

$$\rho = \frac{p}{R_0 T \sum_i Y_i / M_i} \tag{12}$$

where R_0 is the universal gas constant. The internal energy of the mixture is defined as:

$$e = \sum_i \left(Y_i e_i \right) \tag{13}$$

where e_i, the internal energy of the single component gas, is the sum of the energies representing the different degrees of freedom of the molecules. Finally, the enthalpy is:

$$h = \sum_i \left(Y_i h_i \right) \tag{14}$$

Computation of the diffusive fluxes requires knowledge of the transport coefficient.

5.2 Transport properties

For pure species from kinetic theory of gases (Anderson, 1989) follows that:
Viscosity:

$$\mu_i = \frac{2.6693 \times 10^{-6} \sqrt{M_i T}}{\sigma_i^2 \Omega_{\mu i}} \tag{15}$$

Thermal conductivity:

$$\lambda_i = \frac{15}{4} \left(\frac{\mu_i R_0}{M_i} \right) \left(\frac{4}{15} \frac{c_{pi} M_i}{R_0} + \frac{1}{3} \right) \tag{16}$$

Mass diffusivity:

$$D_{ij} = \frac{0.0188 \times T^{\frac{3}{2}} \sqrt{\left(M_i + M_j \right) / M_i M_j}}{p \sigma_{ij}^2 \Omega_{Dij}} \tag{17}$$

Global transport properties of the gas mixture rely on semi-empirical rules such as Wilke's mixing rule for viscosity μ and thermal conductivity λ:

$$a = \frac{\Sigma_i \chi_i a_i}{\Sigma_j \chi_j \left\{ \frac{1}{\sqrt{8}} \left(1 + \frac{M_i}{M_j} \right)^{-\frac{1}{2}} \left[1 + \left(\frac{a_i}{a_j} \right)^{\frac{1}{2}} \left(\frac{M_j}{M_i} \right)^{\frac{1}{4}} \right]^2 \right\}} \qquad a = \mu, \lambda \tag{18}$$

where χ_i is the mole fraction of species *i* and a_i (equal to μ_i or λ_i) is obtained by kinetic theory of gases. For the diffusion coefficient of the i^{th} species in the mixture the multicomponent diffusion coefficient is applied:

$$D_i = \frac{\left(1 - \chi_i \right)}{\sum_j \frac{\chi_i}{D_{i,j}}} \tag{19}$$

with $D_{i,j}$ evaluated by kinetic theory. Finally, vibrational relaxation is modelled using a Landau-Teller formulation, where relaxation times are obtained from Millikan and White, assuming simple harmonic oscillators (Bertin, 1994).

5.3 Chemical species and reactions mechanism

Within a LEO re-entry scenario (e.g., no flowfield ionization occurs), the gas is approximated as a finite-rate chemistry mixture of N_2, O_2, N, O, NO species (Gnoffo et al., 1999). The elementary reactions mechanism, governing the species in high-temperature air, deals with three dissociation reactions and two exchange reactions, as reported in Tables 1a, 1b; there M, namely reacting partner or third body, can be any of the five reacting species, thus providing or removing collision energy. Efficiencies of the third body are also reported in Tables 1a, 1b, since they are employed in computations to increase CPU time efficiency.
The reactions mechanism results in a system of 17 chemical reactions, with 17 forward and backward reactions rate coefficients.

No	Reaction	$A_{f,r}$ (m^3/kgmole s)	$\overline{T}$ (k)	$\beta_{f,r}$	$E_{a\,f,r}$ (J/kgmole)	*Third body efficiency*
1	$O_2 + M = 2O + M$	3.60x10^{15}	T	-1.0	4.947x10^8	O_2=9, N_2=2, O=25, N=NO=1
2	$N_2 + M = 2N + M$	1.90x10^{14}	T	-0.5	9.395x10^8	O_2=1, N_2=2.5, O=N=NO=1
3	$N_2 + N = 3N$	4.085x10^{19}	T	-1.5	9.395x10^8	-
4	NO + M = N + O + M	3.90x10^{17}	T	-1.5	6.277x10^8	O_2=N_2=1, O=N=NO=20
5	$NO + O = O_2 + N$	3.20x10^6	T	1.0	1.638x10^8	-
6	$N_2 + O = NO + N$	7.00x10^{10}	T	0.0	3.159x10^8	-

Table 1a. Reaction rate parameters in Eq. (21), Dunn & Kang model (Gnoffo et al., 1989)

No	Reaction	$A_{f,r}$ (m^3/kgmole s)	$\overline{T}$ (k)	$\beta_{f,r}$	$E_{a\,f,r}$ (J/kgmole)	*Third body efficiency*
1	$O_2 + M = 2O + M$	1.00x10^{19}	T_a	-1.5	4.947x10^8	O_2=N_2=NO=0.2, O=N=1
2	$N_2 + M = 2N + M$	3.00x10^{19}	T_a	-1.6	9.412x10^8	O_2=N_2=NO=0.233, O=N=1
3	NO + M = N + O + M	1.10x10^{14}	T_a	0.0	6.277x10^8	O_2=N_2=0.05, O=N=NO=1
4	$NO + O = O_2 + N$	2.40x10^6	T	1.0	1.598x10^8	-
5	$N_2 + O = NO + N$	1.80x10^{11}	T	0.0	3.193x10^8	-

Table 1b. Reaction rate parameters in Eq. (21), Park model (Park et al., 1993)

Of the simpler sets of homogeneous reactions, it is standard to use the following three chemical reactions, known as Zeldovich process (Sarma, 1995):

$$\begin{aligned} O_2 + N_2 &= 2O + N_2 \\ N_2 + O &= NO + N \\ NO + O &= O_2 + N \end{aligned} \tag{20}$$

It considers only Oxygen dissociation, due to collisions with molecular Nitrogen, and two exchange reactions. This model can be explained considering that the gas is so hot that the Oxygen completely dissociates, while the Nitrogen does neither dissociate completely nor as fast as the Oxygen. Finally, exchange reactions are important because they determine the

speed of Nitrogen dissociation. Chemical reactions proceed with forward rates, $k_{f,r}$ that appear in the source terms ($\dot{\omega}_i$) of the species transport equation, Eq. (9). They are expressed in the Arrhenius form as:

$$k_{f,r} = k_{f,r}\left(\overline{T}\right) = k_f\left(T^a T_v^b\right) = A_{f,r}\overline{T}^{\beta_{f,r}} \exp\left(-\frac{E_{a_{f,r}}}{R_o \overline{T}}\right) \tag{21}$$

where $\overline{T}$ and the constants depend on the model kinetics (see Tables 1a, 1b).
The Dunn-Kang model uses one temperature to describe all the energy modes (e.g. $\overline{T} = T$, thermal equilibrium), while the Park model assumes that $\overline{T}$ can be T, T_v, or $T^a T_v^b$ (namely rate controlling temperature) depending on the reaction (see Table 1b). So Park's two-temperature model provides more accurate results because it uses T to describe translational and rotational energy modes and T_v for vibrational and electron-translational modes.

5.4 Boundary conditions

Eq. (3) states that the properties of a surface are emissivity (ε) and wall catalyticity (i.e. k_{wi}). As atoms of dissociated flow strike vehicle surface, the catalyticity property of the wall is implemented by means of a production term (i.e. $\dot{\omega}_{w\,i} \neq 0$) in the boundary layer problem to solve. Then, steady-state mass atomic conservation at the wall states that the production of i^{th} species, due to the catalytic recombination rate, must be balanced by the rate of diffusion to the surface:

$$\left(\dot{\omega}_a\right)_w = -\left(\rho_a v_a\right)_w \tag{22}$$

The source term $\dot{\omega}_a$ is given by Goulard's relationship:

$$\dot{\omega}_a = k_{wa}\left(\rho_w Y_{iw}\right)^p \tag{23}$$

where p is the reaction order and k_{wi} is the catalytic reaction rate (Anderson, 1989). The diffusive flux $\rho_a v_a$ is expressed by means of Fick's law and then:

$$\left(\dot{\omega}_a\right)_w = k_{wa}\left(\rho Y_i\right)_w^{\ p} = \left(\rho D_a \frac{\partial Y_i}{\partial n}\right)_w \tag{24}$$

When the TPM does not promote any particular reaction (i.e., $\dot{\omega}_{w\,i} = 0$), the TPS surface is called NCW (i.e. $k_{wi}=0$); on the opposite situation, when the TPM can activate any reactions, the TPS surface is called FCW (i.e. $k_{wi}\rightarrow\infty$). Between these two limit cases (i.e. $0<k_{wi}<\infty$), the vehicle surface is considered as PCW and the heat fluxes to the vehicle greatly differ depending on the value of k_{wi}. Furthermore, when a low conductive TPS protects the vehicle, the radiative equilibrium condition holds at vehicle surface. To account for this condition, during numerical simulations, the wall temperature is calculated by Stephan-Boltzman law and is implemented by means of a Newton-Raphson approach.

5.5 Numerical technique

The governing equations, together with the proper boundary conditions, are discretized using a cell-centered finite volume formulation on a structured multiblock grid (see Fig. 3).
For the single-mesh cell, the discretized equation reads:

$$\frac{d\vec{W}_c}{dt}+\frac{1}{V_c}\sum_{f=1}^{6}\left(\vec{F}_{c\,inv}+\vec{F}_{c\,vis}\right)_f\cdot\vec{n}+\frac{\Gamma}{r}\left(\vec{A}^{\,*}_{c\,inv}+\vec{A}^{\,*}_{c\,vis}\right)=\vec{H}_c \tag{25}$$

where f is the index of the cell face and c refers to the single cell of the computational domain. The inviscid fluxes at cell interfaces are calculated by using a flux difference splitting (FDS) Riemann solver, since upwind methods are particularly suitable for high speed flows. However, second order accuracy is not automatically reached. For this reason, a second order essentially non oscillatory (ENO) technique for the reconstruction of cell interface values is employed (Anderson, 1995). The viscous fluxes are calculated by central differencing, i.e. computing the gradients of flow variables at cell interfaces by means of Gauss theorem. The method is second order accurate in space. Time integration is performed by employing both an explicit single-stage (Euler forward) algorithm and an explicit five stage Runge-Kutta scheme, coupled with an implicit evaluation of the chemical and vibrational source terms, under the hypothesis of time marching approach to reach the steady solution for the flow.

6. Reliability of numerical study

A reliable flow simulation dictates the validation of the theoretical models describing the high temperature effects in a hypersonic flow by means of PWT and free flight experimental data. To this end, in order to assess the reliability of present results a numerical rebuilding of ELECTRE (Muylaert et al., 1999) and ARD (Walpot, 2001) test campaigns were performed. Experimental and numerical comparisons of results for both the test models were reported.

6.1 ELECTRE test article in HEG wind-tunnel

ELECTRE test article (see Fig. 4) consists of a blunt conical surface 0.4 m long, semiaperture cone angle of 4.6° deg, and hemispherical nose radius of 0.035 m. It was tested in flight and in PWT, becoming a standard reference model to study non-equilibrium hypersonic flow past blunt-body configurations (Muylaert et al., 1999). The CFD computational domain, shown in Fig.4, consists of 60x120 cells with a minimum normal wall spacing of 10^{-5}m which a grid sensitivity analysis has shown to be necessary to obtain a sufficient resolution of the flowfield features.

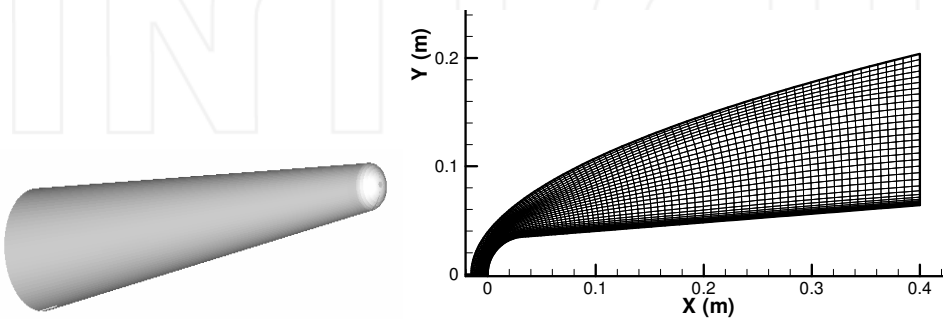

Fig. 4. ELECTRE test article geometry and axi-symmetric mesh domain

Test conditions are summarized in Tab.2. They correspond to operating conditions of the HEG PWT located at DLR Gottingen at which two different test cases were run considering alternatively the specimen wall as NC, and FC for N and O species.

T_∞	P_∞	ρ_∞	V_∞	M_∞	Re_∞/m	Y_O	Y_N	Y_{NO}	Y_{O2}
(K)	(Pa)	(kg/m^3)	(m/s)	(-)	(1/m)	(-)	(-)	(-)	(-)
790	430	$1640x10^{-6}$	5919	9.7	$270x10^3$	0.179	$1.0x10^{-6}$	$3.3x10^{-2}$	$3.6x10^{-2}$

Table 2. Reference calibration point conditions of the HEG nozzle (Muylaert et al., 1999)

As an early assessment of work several engineering evaluations have been accomplished by means of ENTRY as, for example, pressure coefficient and convective heat transfer distributions on the test article wall. ENTRY quickly evaluates the pressure distribution by using the surface impact method, typical of hypersonics:

$$C_p = C_{pt2}\,\mathrm{sen}^2\theta \tag{26}$$

where Cp_{t2} is the stagnation-point pressure coefficient that depends on the flow theory one considers, while θ is the local slope body angle (Bertin, 1994). For example, Newtonian flow theory states that Cp_{t2} is equal to 2 while in the case of Modified Newtonian theory (see Eq.(1)) it reads:

$$C_{pt2} = \left(\frac{P_{t2}}{P_\infty} - 1\right)\frac{2}{\gamma M_\infty^2} \tag{27}$$

For the aeroheating, ENTRY evaluates the convective heat transfer around both hemispherical nose and spherically capped cone, according to the Lees theory (Lees, 1956). Lees approach shows that, for a blunt cone with nose radius R_N and semiaperture vertex angle θ_c, at any point on the cone surface, the ratio of heat transfer to the stagnation value $\dot{q}_{co}$ reads:

$$\begin{aligned} &\text{Nose} && \frac{\dot{q}_w(\theta)}{\dot{q}_{co}} = \frac{2\theta\sin\theta\cos^2\theta}{\sqrt{D(\theta)}} \\ &\text{Cone skirt} && \frac{\dot{q}_w(s')}{\dot{q}_{co}} = A(\theta_c)\frac{s'}{R_N}\left[B(\theta_c) + \left(\frac{s'}{R_N}\right)^3\right]^{-\frac{1}{2}} \end{aligned} \tag{28}$$

Eq.(28) is valid for $s'/R_N \geq \cot\theta_c$, where s' is the curve length measured along the cone surface of the effective sharp-nosed cone and, for high flight Mach number:

$$\begin{aligned} A(\theta_c) &\approx \frac{\sqrt{3}}{2}\sin\theta_c\sqrt{\frac{\pi}{2} - \theta_c} \\ B(\theta_c) &\approx \frac{3}{16}\frac{1}{\sin^4\theta_c}\left[\frac{D(\theta)}{\theta}\right]_{\theta=\frac{\pi}{2}-\theta_c} - \cot^3\theta_c \\ D(\theta) &\approx \theta^2 - \frac{1}{2}\theta\sin 4\theta + \frac{1}{8}(1 - \cos 4\theta) \end{aligned} \tag{29}$$

CFD aerothermodynamic computations have been performed with different wall catalytic boundary conditions for the test article. The computations refer to fully laminar non-equilibrium flow conditions with model temperature fixed to T_w=300 K.
The flowfield past the test bed is shown in Fig.5, where the Mach number contour field is plotted, comparing the results for perfect gas (upper side) and real gas model (lower side).

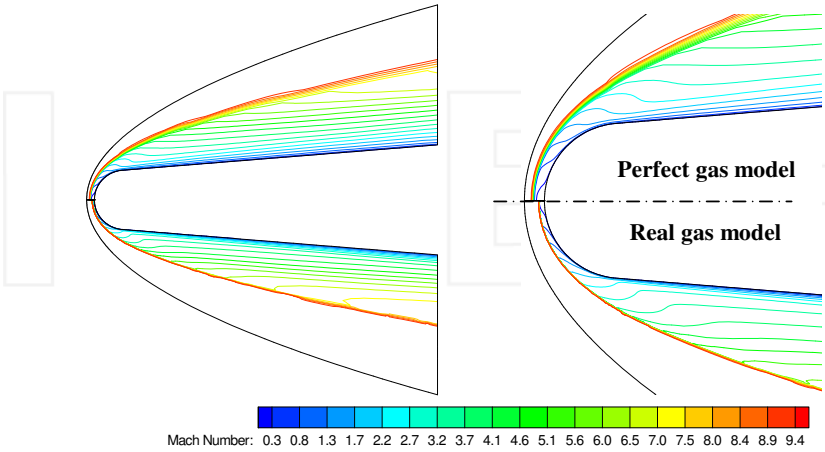

Fig. 5. Mach number contours field. Comparison between perfect gas (top) and real gas model. Detail on the nose region of the test bed (right)

Pressure coefficient and wall heat flux distributions for different wall catalytic conditions are reported respectively in Fig. 6 and Fig. 7, where CFD results were compared with engineering and available experimental results (i.e. shot157, shot159, shot164) (Muylaert et al., 1999).
The Cp comparison of numerical, experimental and engineering results shows good agreement in the first part of the test specimen, with differences only at the model end. In particular, Fig. 6 highlights that no differences exist between NC and FC wall boundary conditions, as expected. Moreover, ENTRY results (see Fig. 6-b) compare well with the Modified Newtonian theory, where the Cp_{t2} has been evaluated using the inflow specific heat and Mach number as provided by CFD analyses. As shown, the pressure on the probe nose decreases with curve length from the stagnation point, becoming constant on the conical skirt (e.g., $\theta=\theta_c$=const in Eq.(26)). Modified Newtonian theory, however, loses in accuracy as highlighted by CFD since the surface pressure depends on many factors such as the interaction of compression and of expansion waves which originate from body curvature, reflection from the bow shock and slip lines due to the rotationality introduced by the curved bow shock wave. In particular, as the cone is very slender, the surface pressure in the expanding flow decreases so slowly that the asymptotic (sharp cone) value is not reached, resulting in an underexpanded flow. The heat flux distribution (see Fig. 7) shows an agreement with the numerical FC solution (the red curve) on the nose of the test article while on the rear part of cone there is a mismatch between experimental data and CFD results, as already seen in the case of Cp. Both these mismatches could be probably caused by flowfield perturbations due to the support arm, located at the end of the test bed. Anyway Fig.7-b shows that CFD results compare well with Lees theory.

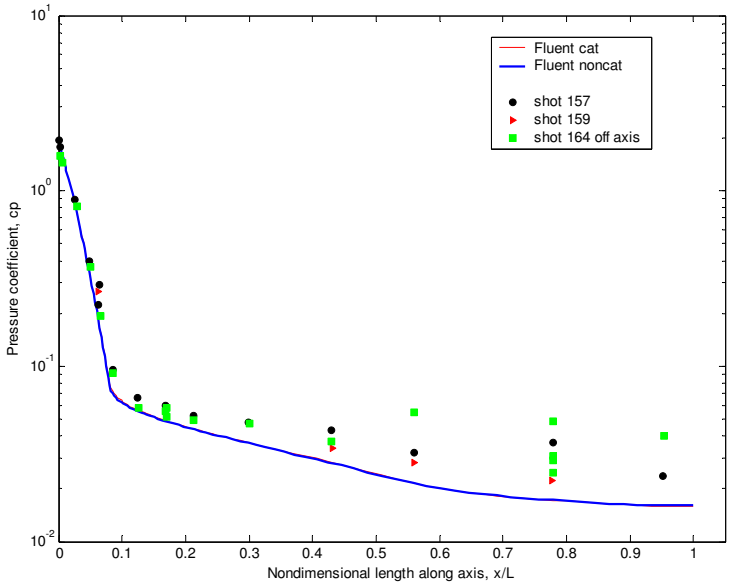

a)

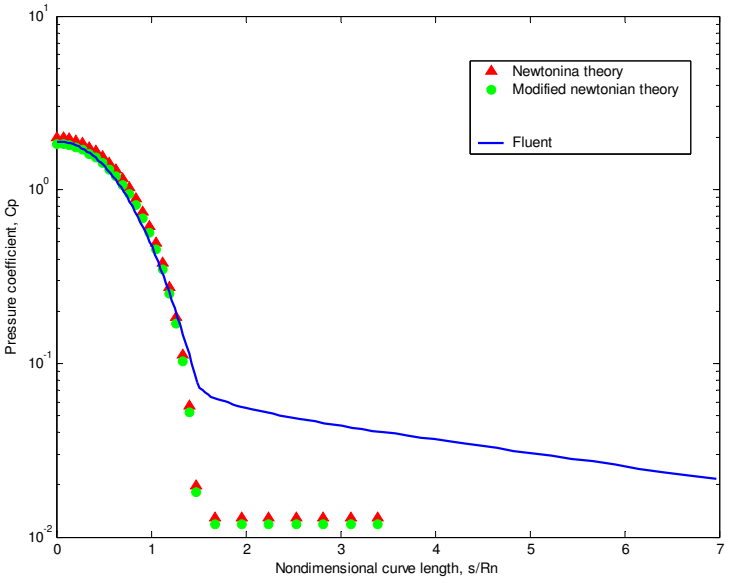

b)

Fig. 6. a) Cp comparison between numerical, engineering, and experimental data, b) detail on the nose probe (Muylaert et al., 1999)

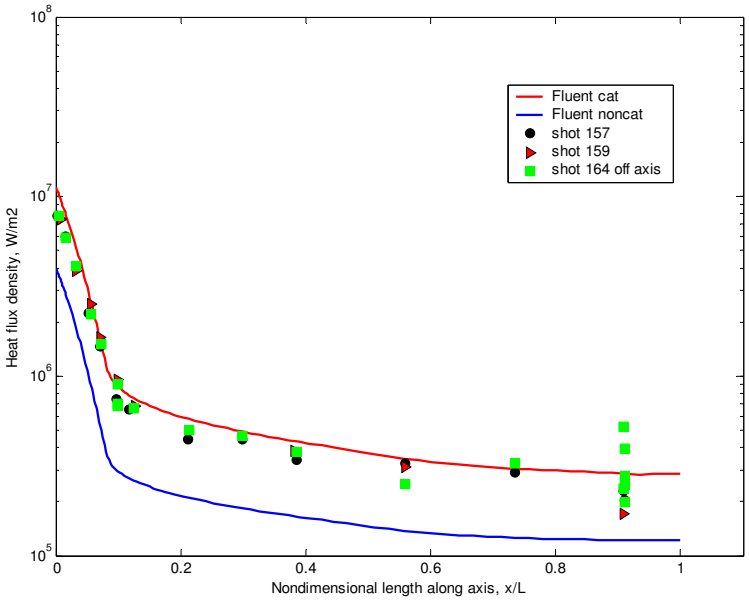

a)

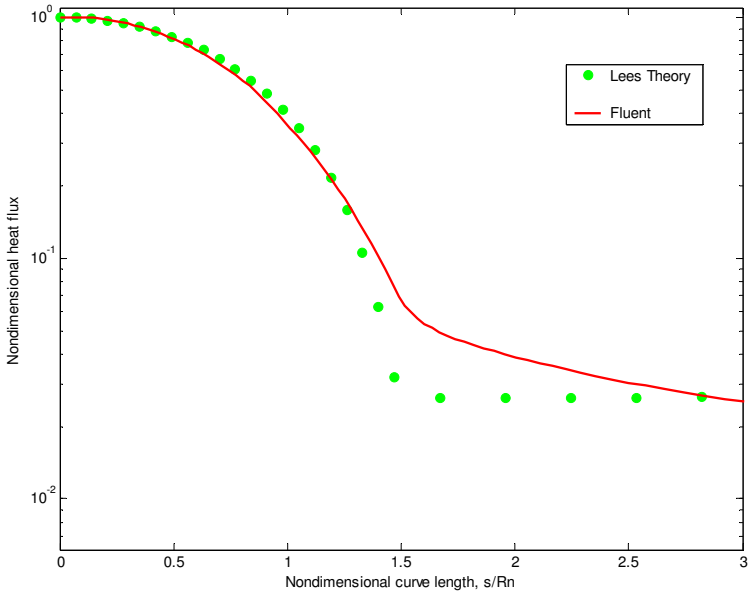

b)

Fig. 7. Heat flux; a) comparison between numerical, engineering, and experimental data; b) detail on the nose probe (Muylaert et al., 1999)

6.2 ARD model in S4 wind-tunnel

S4 test campaigns provide pressure profiles on the forebody centerline of the atmospheric re-entry demonstrator (ARD) capsule (see Fig.1) at the freestream conditions of Tab. 3 (Walpot, 2001).

P_0 (bar)	85	25
T_0 (k)	1151	1108
$Re_{D\infty}$	967237.3	319208
M_∞	9.92	9.72
P_∞ (Pa)	211.3	71.17
T_∞ (k)	55.7	55.7
T_{wall} (k)	300	300
X_{cg}/D	0.26	0.26
Y_{cg}/D	0.0353	0.0353
AoA (deg)	-20	-20

Table 3. ONERA S4 exit conditions (Walpot, 2001)

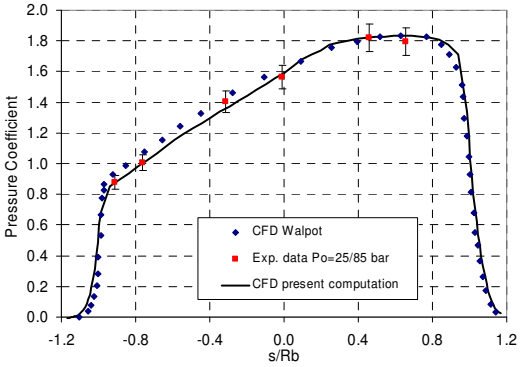

Fig. 8. Pressure coefficient: comparison between present results and data in (Walpot, 2001)

Results of present computations in terms of Cp on forebody centerline are summarized and compared with experimental data in Fig. 8, where CFD data provided by Walpot are also reported as further benchmark (Walpot, 2001). As one can see, experimental and numerical data compare well, thus confirming the reliability of numerical results.

7. CRV flowfield computational analysis

Axi-symmetric and fully three-dimensional simulations were performed at the freestream conditions listed in Table 4, with the far field composed of 79% N_2 and 21% O_2.

In order to appreciate how vehicle flowfield depends on real gas effects, numerical computations have been performed in a step-by-step approach. For instance, starting with the perfect gas model, flowfield computation accounts for the chemistry considering first the flow in equilibrium conditions and then in non-equilibrium ones. In the latter case, the effects of both reaction mechanism and chemical kinetics are considered, for example, by means of Zeldovich reaction mechanism, and Dunn-Kang and Park kinetic models. Finally,

thermal non-equilibrium and wall catalyticity are accounted for, providing a complete overview of high temperature effects on CRV aerodynamics and aerothermodynamics.

Altitude (Km)	Mach (-)	Pressure (Pa)	Temperature (k)	AoA (deg)
50	10	79.78	270.65	0
57	19	32.78	255.27	10
57	19	32.78	255.27	17.5
57	19	32.78	255.27	21
57	19	32.78	255.27	28
57	16	32.78	255.27	28
57	12	32.78	255.27	28

Table 4. Freestream conditions of CFD computations

All the computations considered in this work have been performed by means of an Intel Core Duo E7300 at 2.66 GHz.

7.1 Axi-symmetric computations

A general overview of the flowfield past the vehicle is shown in Fig. 9, where contours of pressure and translational temperature in the forebody flowfield are plotted. They refer to a perfect gas computation performed at M_∞=19, H=57 km and α=0 deg (e.g., peak heating conditions of the ballistic trajectory of Fig. 2).

Figure 10 shows a comparison of the non-dimensional temperature profile between perfect gas (PG), equilibrium gas (EG), chemical non-equilibrium gas with NCW and chemical non-equilibrium gas with FCW, as evaluated along with the stagnation line. As clearly shown, the temperature is large enough to cause the complete Oxygen dissociation in the shock layer while Nitrogen partially dissociates. Moreover, differences can be found in temperature peak, stand-off distance and also in the equilibration trend for translational temperature. In particular, in the case of chemical non-equilibrium computation, the temperature profile on the stagnation line exhibits a sharp discontinuity at the shock wave and a large overshooting value due to the finite rate dissociation of molecules.

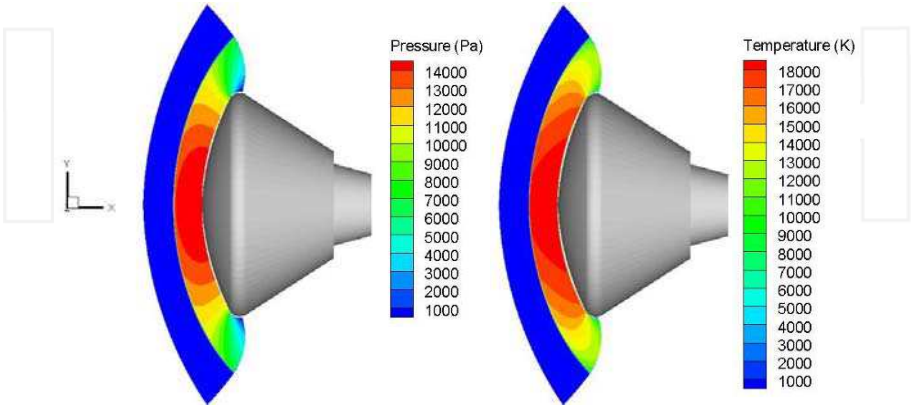

Fig. 9. Contours of static pressure (left) and temperature for α=0 deg, M_∞=19, and H=57 km

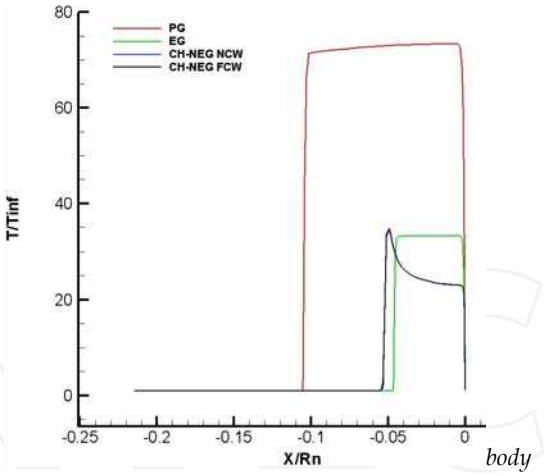

Fig. 10. Comparison of static temperature for α=0 deg, M_∞=19, and H=57 km, along with the stagnation line for different chemical models

Figure 10 also shows that the shock layer becomes thinner because high temperature phenomena absorb heat, thus decreasing the effective specific heat ratio γ. As a result, the gas compressibility changes, which lead to changes in the shock wave shape around the vehicle. In particular, as the green curve highlights, this phenomenon occurs more prominently in the equilibrium flow than in a non-equilibrium one.
When we account for the influence of chemical kinetics, we have provided in Fig. 11 the comparison of non-dimensional temperature profiles, along the stagnation line, for the results of Dunn-Kang and Park models.

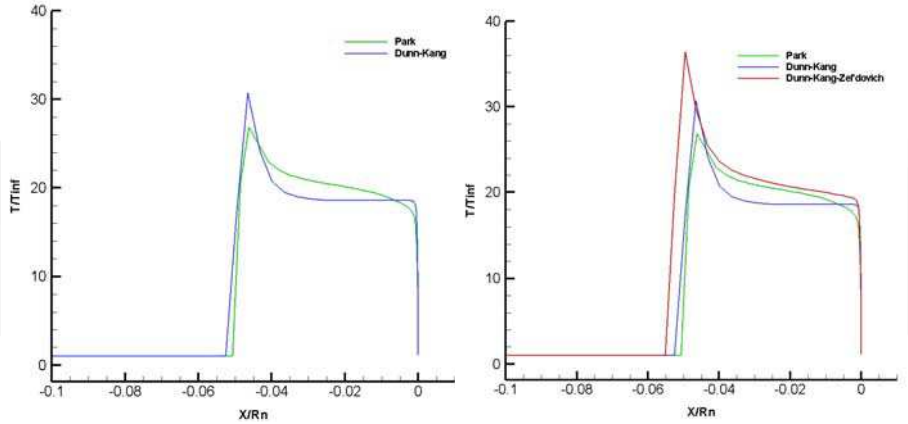

Fig. 11. Comparison of translational temperature, along the stagnation line, for different chemical models and reaction mechanisms, for α=0 deg, M_∞=19, and H=57 km.

As shown, chemical kinetics slightly changes both stand-off distance and the peak temperature. Differences are also in the shape of temperature profiles in the shock layer,

because for the Dunn-Kang model the flow equilibrates before reaching the boundary layer, differently from the case of Park model. As to the effects of the reaction mechanism, Fig. 11 (right side) also reports the effect of the Zeldovich's model on translational temperature along the stagnation line. As one can see, this reaction mechanism over-estimates both temperature peak and stand-off distance. In particular, the temperature profile of complete reaction mechanism (the blue curve), shows that flowfield in the shock layer tends toward equilibrium faster than Park and Zeldovich results.

The effects of vibrational relaxation can be appreciated in Fig. 12, where the comparison between translational temperature distributions, along the stagnation line, is reported for Park kinetics.

Results shows only slight differences between the case of thermal equilibrium and non-equilibrium computation. When vibrational equilibrium holds (green curve) there is no incubation time for vibration to relax, as highlighted by the temperature rise of the curve. Therefore, we can conclude that at the peak heating the flowfield around the capsule is characterized by an almost thermal equilibrium conditions (remember that capsule features a large forebody radius, R_N=6.05 m). Hence, chemistry is active just behind the shock and energy goes only in chemistry thus yielding lower translational temperature in the shock layer. In fact, even if the exact functional dependence is unknown, it is agreed that a reaction mechanism depending only on T over-predicts the amount of dissociation.

Thermal equilibrium conditions are also confirmed by results summarized in Fig. 12 (right side), where the comparison between the translational and vibrational non-dimensional temperatures is reported.

As we can see, temperature profiles are almost overlapping except across the shock, with the vibrational temperature of molecular nitrogen that slightly lags behind the others (e.g., the energy transfer takes a certain number of collisions to proceed). In particular, O_2, NO and N_2 quickly equilibrate.

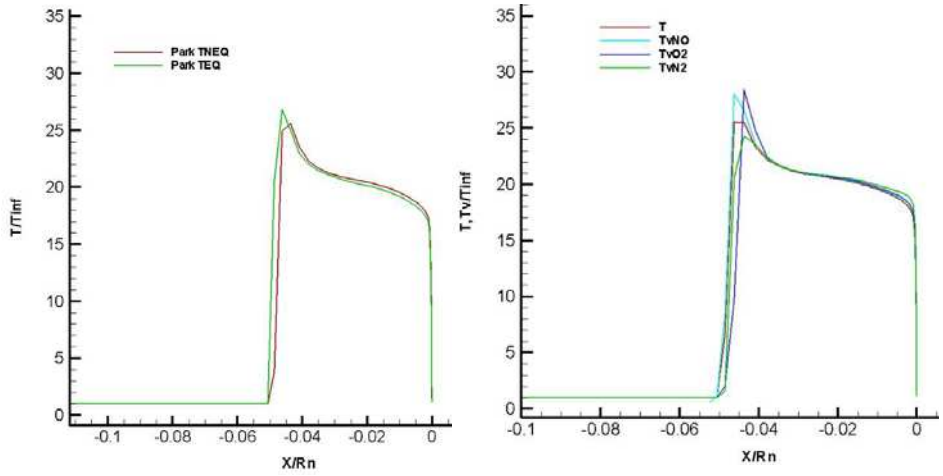

Fig. 12. Translational and vibrational temperatures along with the stagnation line for α=0 deg, M_∞=19, and H=57 km for NCW. Comparison between thermal equilibrium (TEQ) and non-equilibrium (TNEQ) conditions for Park kinetics

7.2 Three-dimensional computations

In the framework of 3-D CFD computations, several AoAs have been considered (see Tab.4). Figure 13 shows the static temperature contours on capsule symmetry plane and two flowfield cross sections and the static pressure contours on the CRV surface at M_∞=19 and α=20 deg, considering the flow as a reacting gas mixture. As shown, the CRV bow shock structure around the descent vehicle can be appreciated as well. Figure 14 reports the flowfield contours of Oxygen (O) and Nitrogen (N) mass fraction (on the right side) for M_∞=19, H=57 km, and α=20 deg. As expected, the oxygen is fully dissociated.

Concerning capsule static stability, the transition in sonic line location is shown in Fig. 15 to Fig. 17 for different AoA and Mach numbers. Figure 15 reports sonic line location for four cases, involving two different Mach numbers (e.g., 10 and 19) and all the AoA considered in the computations. As shown, the sonic line location and its shape markedly depend on freestream Mach number, altitude and AoA, thus highlighting that capsule attitude conditions are highly influenced during descent.

In order to appreciate the effect of finite rate chemistry, the sonic line comparison between PG and RG computations both for M_∞=16 and M_∞=19 is summarized in Fig. 16.

In both cases for the PG solution the flowfield around almost all the capsule heat shield is entirely subsonic with consequent high pressure distribution. Therefore, as the sonic line shifts due to the chemical reactions, the flow becomes entirely supersonic and the pressure decreases, thus confirming that pitching moment (CM_y) and α_{trim} are affected by real gas effects. In particular, differences between the green and blue lines on the capsule afterbody, underline that at M_∞=19 CM_y is affected by the chemical kinetics while no influences are expected when CRV is flying at M_∞=16 (see left side of Fig. 16).

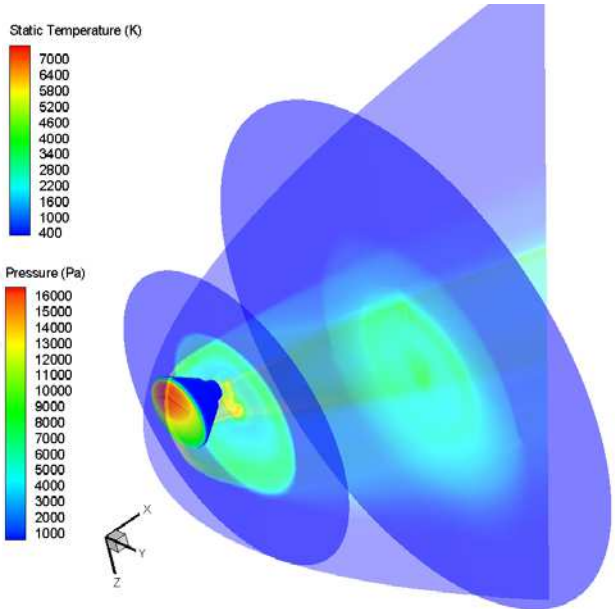

Fig. 13. Static temperature on CRV symmetry plane and two cross sections at M_∞=19, H=57 km and α=20 deg. Static Pressure contours on capsule forebody

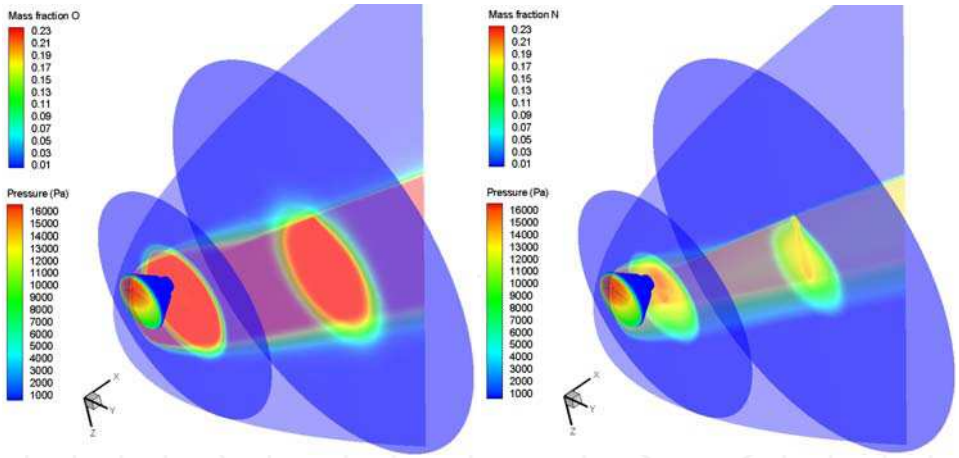

Fig. 14. Flowfield contours of Oxygen and Nitrogen (right) mass fraction for M_∞=19, H=57 km, and α=20 deg on CRV symmetry plane and two cross sections. Static Pressure contour on capsule forebody

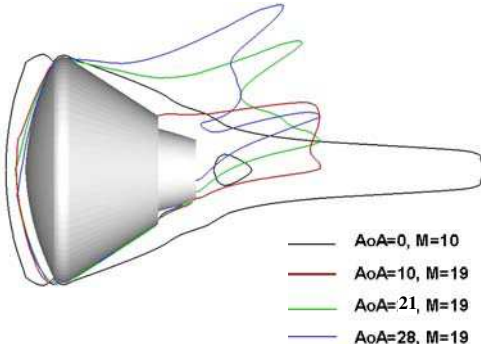

Fig. 15. Sonic line location in the capsule pitch plane for different AoA and Mach number

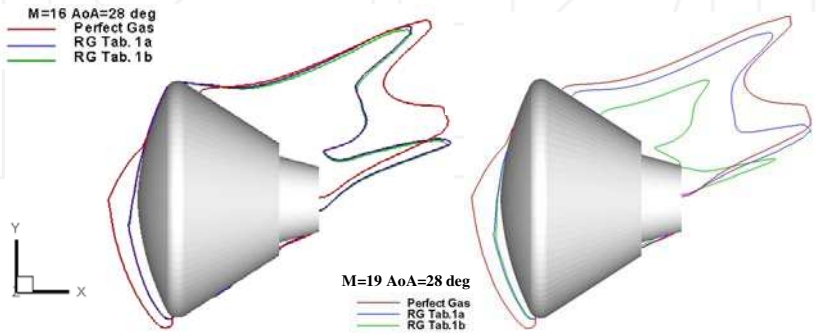

Fig. 16. Sonic line location in the capsule pitch plane for M_∞=16, M_∞=19, H_∞=57 km and α=28 deg. Comparison between PG and RG computations

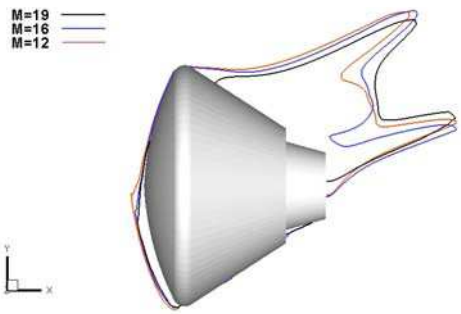

Fig. 17. Sonic line location in the capsule pitch plane at α=28 deg and H_∞=57 km. Comparison among M_∞ =12, 16 and 19

Finally, Fig. 17 shows the sonic line for M_∞=12, 16, and 19 at the same α, thus highlighting the effect of the Mach number. Therefore, region of vehicle static instability could be expected during re-entry, depending on the capsule's c.g. location.

8. CRV aerodynamic analysis

Aerodynamic features of primary interest for an axi-symmetric vehicle are lift (C_L), drag (C_D), and pitching moment (CMy) coefficients, which are calculated according to Eq. (30).

$$C_i = \frac{F_i}{\frac{1}{2}\rho_\infty v_\infty^2 S_{ref}} \quad i = L, D \qquad C_{M\,j} = \frac{M_j}{\frac{1}{2}\rho_\infty v_\infty^2 L_{ref} S_{ref}} \quad j = Y \tag{30}$$

where L_{ref}=5.0 m (i.e., CRV diameter–longitudinal reference length); $S_{ref}=(\pi D^2)/4$=19.6 m^2 (i.e. CRV maximum cross-section area). Pole coordinates for the CM_y calculation are (1.3,-0.1765,0) m (i.e., vehicle cg). Based on the reentry scenario of Fig. 2 the AEDB has been generated for FMF, transitional regime and continuum flow. No lateral directional analysis has been taken into account in this work. CRV aerodynamic appraisal within FMF and transitional regime entails Direct Simulation Monte Carlo Method (DSMC) computations and a very simple relationship to bridge the transitional flow regime from continuum to FMF one (Pezzella et al., 2009). CRV continuum aerodynamics refers to both engineering-based analysis and CFD-based analysis.

8.1 Engineering-based aerodynamics of CRV

As an early assessment of the CRV continuum aerodynamics several engineering evaluations have been accomplished by ENTRY considering that when the capsule travels at hypersonic velocities the aerodynamic forces are dominated by pressure effects. Viscous and other effects, such as base drag, represent only about ten percent of the total. So the flow may be approximated as inviscid and surface inclination methods (SIM), like Modified Newtonian theory (MN), can be used (Bertin, 1994). To this end let us consider Fig.18 where the capsule's outer mold line (OML) is shown.

Assuming that the freestream particles impact only on the frontal area of the body and cannot curl around it, combining Eq. (26) and Eq. (1), MN theory suggests that the pressure coefficient (C_p) becomes:

$$C_P = (2-\varepsilon) sen^2\theta \tag{31}$$

By integrating Eq. (31) over the whole vehicle surface one is able to evaluate aerodynamic forces acting on the vehicle, both for zero lift and AoA cases.

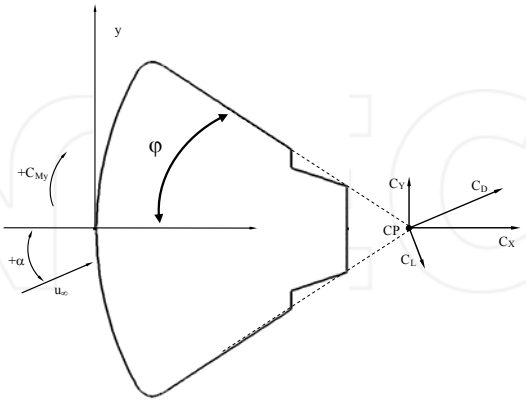

Fig. 18. Capsule OML used for surface impact method aerodynamics

8.1.1 Zero lift aerodynamics

The zero lift drag coefficient of the CRV is given by:

$$C_{Do} = \frac{2\pi}{S_{ref}} \int_0^{\varphi} C_P\, r^2 \sin\varphi \cos\varphi\, d\varphi = \frac{(2-\varepsilon)}{2}\left(1+\cos^2\varphi\right) \tag{32}$$

where φ is the capsule frustum angle (i.e. 33 deg).

8.1.2 AoA aerodynamics

When the capsule is flying at an AoA the pressure coefficient on vehicle's wall facing flow, reads:

$$C_P = (2-\varepsilon)\left(\hat{u}\cdot\hat{n}\right)^2 = (2-\varepsilon)\left(\cos\alpha\cos\theta + \sin\alpha\sin\theta\right)^2 \tag{33}$$

So, when α <θ (i.e. the sidewall surface is shadowed) the axial and normal force coefficients are, respectively:

$$C_X = \frac{(2-\varepsilon)}{2}\left[cos^2\alpha\left(1+cos^2\varphi\right) + \frac{1}{2}sen^2\alpha\, sen^2\varphi\right] \tag{34}$$

$$C_Y = \frac{(2-\varepsilon)}{2} cos\alpha\, sen\alpha\, sen^2\varphi \tag{35}$$

Therefore, the capsule lift to drag ratio (E) is:

$$E = \frac{C_L}{C_D} = \frac{C_Y \cos\alpha - C_X \text{sen}\alpha}{C_Y \text{sen}\alpha + C_X \cos\alpha} \tag{36}$$

By imposing the pitch moment balance around the vehicle heat shield nose we have:

$$CM_Y = -\frac{x_{cp}}{L_{ref}} C_Y = -\frac{(2-\varepsilon)}{2L_{ref}} x_{cp} \cos\alpha \,\text{sen}\alpha \,\text{sen}^2\varphi \tag{37}$$

where x_{cp} is the abscissa of the vehicle center-of-pressure (cp) that, as said before, is expected to be influenced by the real gas effects, thus affecting capsule trim angle and in turn its descent flight due to the lower aerodynamic efficiency of vehicle (Park et al., 1992). Then, for very high Mach numbers, say larger than five, SIM states that the aerodynamic characteristic of the capsule does not depend on vehicle velocity, but rather on the α and the geometric angle of the body shape φ. Further expressions to compute lift and drag coefficients are:

$$C_D = C_{Do} + 12(1 - C_{Do}) sen^2 \frac{\alpha}{2} - 6(6 - 5C_{Do}) sen^4 \frac{\alpha}{2} + 4(6 - 5C_{Do}) sen^6 \frac{\alpha}{2} \tag{38}$$

$$C_L = \left[2(1 - C_{Do}) - (3 - \frac{5}{2} C_{Do}) sen^2\alpha \right] sen\alpha \tag{39}$$

8.2 CFD-based aerodynamics of CRV

Curves of aerodynamic efficiency and pitching moment coefficient are shown in Fig. 19. Note that, CM_Y, shows that the pitching moment derivative CM_α is negative in the AoA range of 150-180 deg, signifying that the CRV is statically stable for this range of α (provided that the capsule cg is close to the moment reference point).

Other numerical data, provided in (Crowder et al., 1969), are also reported to highlight the accuracy of results. As to the effect of chemical kinetics on CRV aerodynamics, Fig. 20 shows that at M_∞=16 no differences are expected for aerodynamic forces, passing from Dunn-Kang to Park kinetics. On the contrary, at M_∞=19 both C_L and C_D increase ranging from PG through DK and Park kinetics. Differences of about 2% and 5% are observed concerning the value of C_L and CM_Y, respectively. These conclusions for M_∞=19 are confirmed by the displacement of the abscissa of the vehicle centre-of-pressure (x_{cp}) non-dimensionalized with respect to its value for MN (Viviani et al., 2010). The increase in Cp at the stagnation region and its decrease over the remaining region lead to a forward (toward nose) shift of centre-of-pressure, or equivalently, positive (nose-up) pitching moment, as the flow γ decreases.

Figure 20 also shows that at M_∞=16, the x_{cp} in the case of PG solution decreases of about 10% with respect to the MN estimation and there are no differences between the values provided by both the chemical models. At M_∞=19, instead, even if the value of x_{cp} in the case of PG solution decreases again of about 10% with respect to the MN estimation, the two chemical models provide values that differ from each other of about 2%. Note that the latter difference may be dangerous if neglected when designing vehicle thermal shield layout. Analyses of the effect of chemical kinetics on capsule aerodynamics at α=28 deg versus Mach number, can be found in (Viviani et al., 2010).

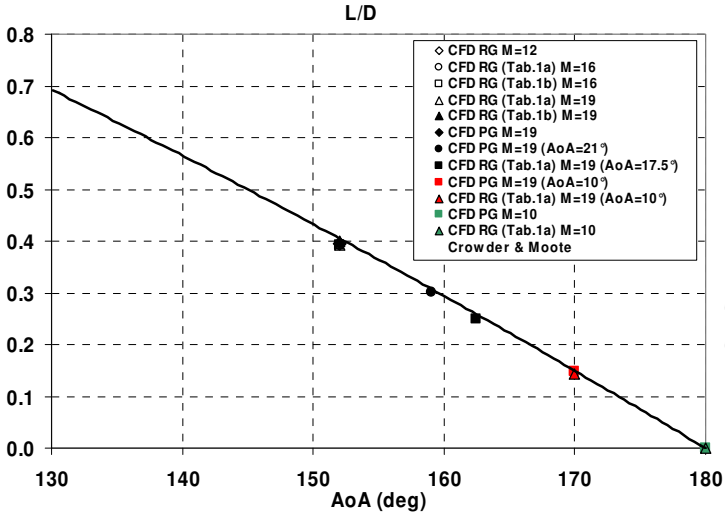

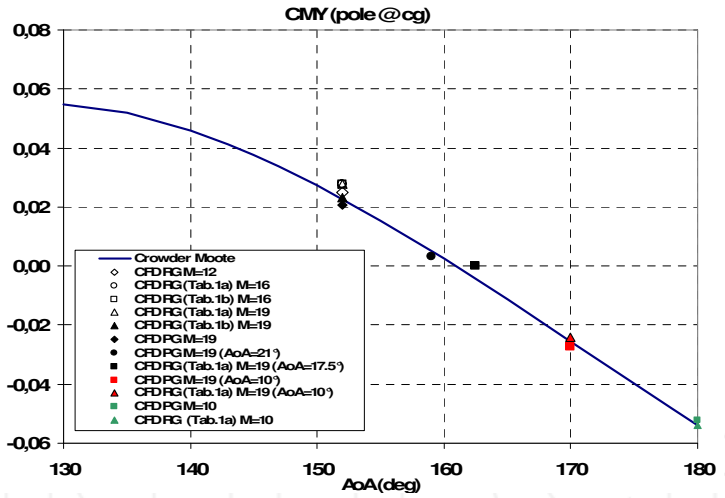

Fig. 19. Capsule L/D and CM_y versus α. Comparison among present and literature data (Crowder et al., 1969)

Finally, Fig. 21 shows, in a step-by-step approach, the effects of reaction mechanism on CRV aerodynamics when the capsule is flying at α=28 deg, M_∞=19 and H=57 km.
As shown, the results for Zeldovich model compare globally well with those of the complete reaction mechanism, i.e. 17 reactions. Such a result is very interesting considering that Zeldovich results differ from those of full reaction mechanism of 1% only for all the aerodynamic coefficients. In this case, in fact, the CPU time efficiency increases of about 40 %. Therefore, the gain in terms of solution speed up is very high if compared to the loss in

accuracy of 1% only. The same consideration can be made in the case of aerodynamic results obtained in the case of O_2, N_2 and NO dissociation only, even if here the CMy differs of about 5 %. When results refer to O_2 and N_2 dissociation only, CPU time efficiency increases of about 45% but the CMy accuracy evaluation is in the range of 10%. Finally, when aerodynamic coefficients account for only O_2 dissociation the speed up efficiency reaches about 65%, whereas when flow dissociation is neglected (e.g., PG solution) the gain is nearly 70%. In this case, however, CMy differs of about 15% and 25%, respectively. As a result, Fig. 21 highlights that CPU speed up depends on the accuracy expected in vehicle pitching moment assessment. Therefore, this confirms that CMy is one of the most critical parameters within vehicle aerodynamic design.

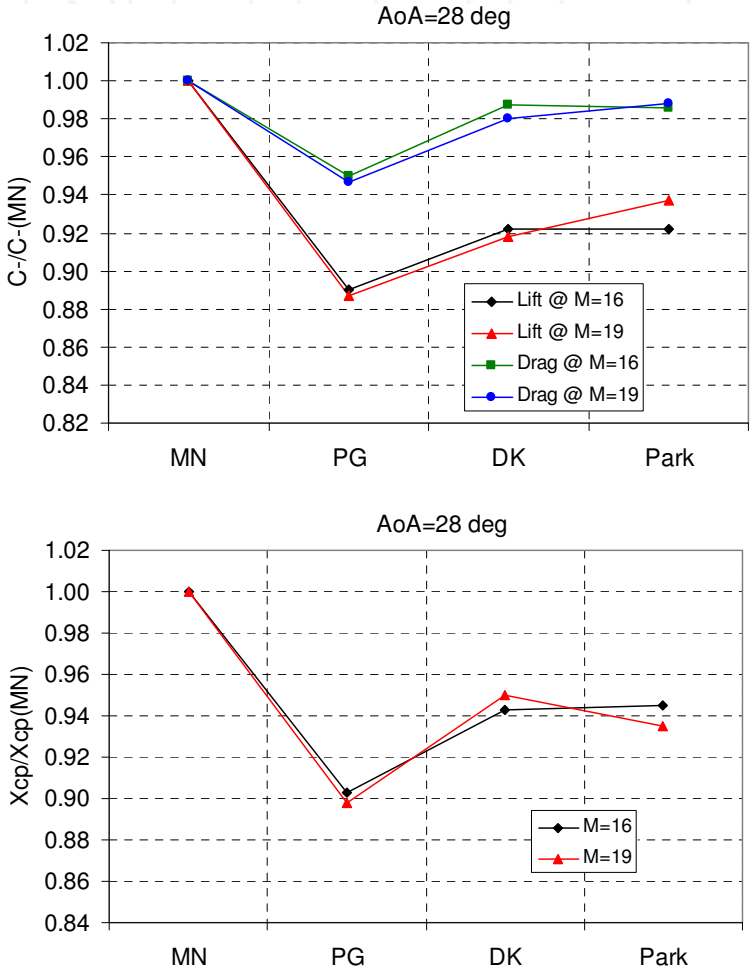

Fig. 20. Effect of chemical reactions on CRV aerodynamics at α= 28 deg for M_∞=16 and M_∞=19. Comparison among MN, PG, Dunn-Kang and Park computations

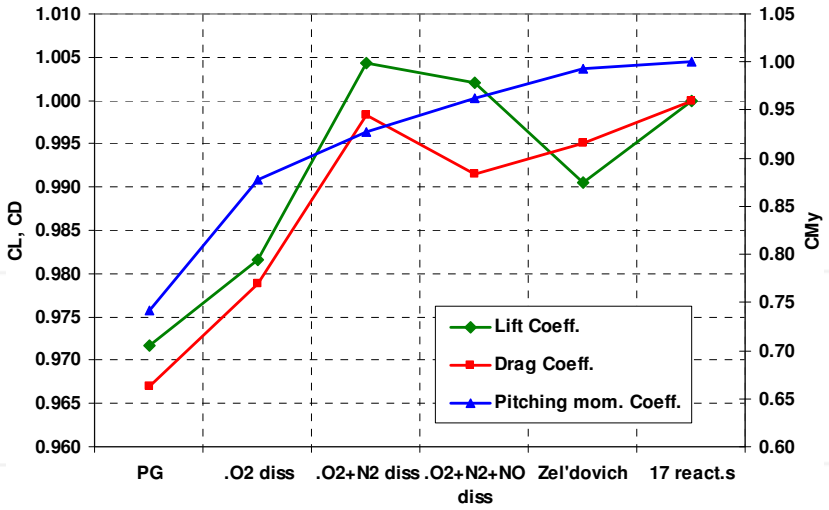

Fig. 21. Effects of reaction mechanism on CRV aerodynamics at α=28 deg, M_∞=19 and H_∞=57 km

8.3 Free molecular flow and transitional aerodynamics of CRV

Drag coefficients, evaluated by means of DSMC simulations, have been reported and compared in Fig. 22, with those assessed through a quick engineering estimation provided by a bridging relationship between FMF results and continuum ones. For instance, a very simple relationship to bridge the transitional flow regime from continuum regime to FMF reads:

$$C_{D\,Transitional} = C_{D\,Continuum} + \left(C_{DFM} - C_{D\,Continuum}\right) \cdot \bar{C}_D \tag{40}$$

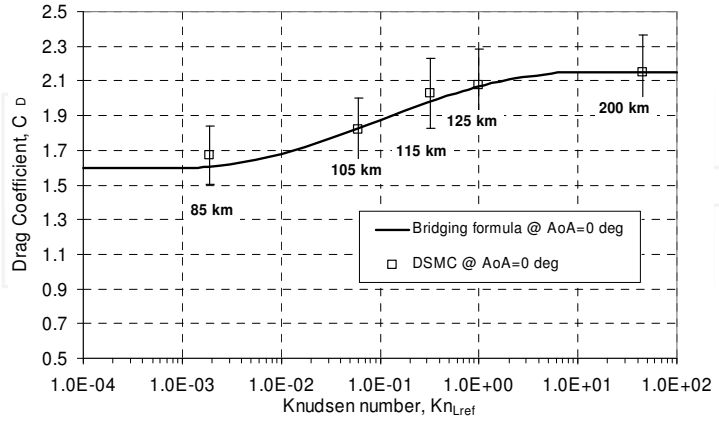

Fig. 22. Drag coefficients vs Knudsen number for α=0 deg (Pezzella et al., 2009)

where the normalized coefficient $\bar{C}_i$ uses Knudsen number as the independent parameter:

$$\bar{C}_D = \frac{C_D - C_{DContinuum}}{C_{DFM} - C_{DContinuum}} = F(Kn_\infty) = sen^2\left[\frac{\pi}{8}\left(3 + Log_{10}Kn_\infty\right)\right] \quad (41)$$

10-3<Kn∞<10 and $C_{DContimuum}$ and C_{DFM} are the aerodynamic drag coefficient in continuum and FM flow regimes, respectively.

The effect of rarefaction on the aerodynamic drag is clearly shown considering that C_D at α=0 deg increases of about 24% passing from 85 km to 125 km, whereas the drag at H=200 km is 25% higher than the one at 85 km.

9. CRV aerothermodynamic features

The CRV aeroheating analysis reveals two critical regions on the vehicle surface (Viviani et al., 2007). They are the stagnation point (capsule flying at α=0 deg) and the vehicle side corner (capsule flying at α≠0 deg).
Several Navier-Stokes computations have been performed assuming the chemically reacting gas model, considering alternatively the heat shield surface as NC, PC and FC wall. The computations refer to fully laminar flow conditions with capsule surface temperature fixed at 300 K or in radiative equilibrium conditions. Note that, due to relatively low entry velocities (e.g., no radiation heat flux applies) only convective heat flux are taken into account. Moreover no heat shield ablation and recession were assumed for simplicity.
In order to illustrate the high temperature real gas effects in air, Fig. 23 shows the comparison of heat flux on the forebody centerline, in the cases of PG, EG and chemical non-equilibrium gas; for the latter case, the results for NCW and FCW are also reported. All these heat flux profiles are evaluated for cold wall conditions (e.g., T_w=300 K).

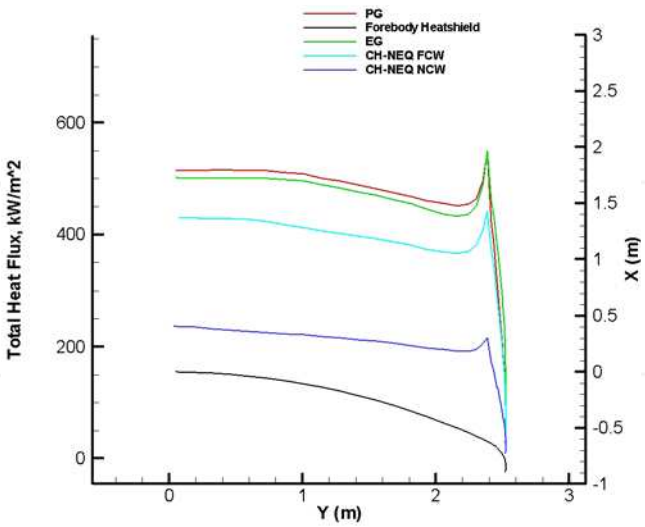

Fig. 23. Real gas effect on CRV forebody heat flux at α= 0 deg, M_∞=19 and H_∞=57 km. T_w=300 K

As shown, the wall heat flux is higher in the case of chemical equilibrium condition and it is closer to the heat flux for PG simulation. This can be explained considering that as the wall is cold, the chemical equilibrium leads to the recombination of dissociated atoms.
When the boundary layer (BL) is in chemical non-equilibrium, CFD simulations confirm that the higher heat flux is attained for FCW. As shown, this value is lower than that for EG, but it is very large compared with the case of NCW, as expected. Therefore, we can conclude that if the gas in the BL is in equilibrium (e.g., fast recombination) then a surface catalyst will not have any effect on the formation of molecules. In this case, in fact, atoms recombine and liberate their energy of dissociation to the gas in the BL. This added heat tends to increase the heat flux to the surface via thermal conduction, thus indicating that the recombination of atoms is more important than in the case of a FCW. For this reason, we regard the equilibrium condition as the reference condition in much of the state of the art TPS design activities.
The equilibrium condition hypothesis, however, may lead to an excessively conservative assessment of vehicle aeroheating. Therefore, realistic heat flux assessment over vehicle surface demands non-equilibrium flowfield computations with a full reaction mechanism, as wall catalyticity plays a significant role when assessing vehicle aeroheating.

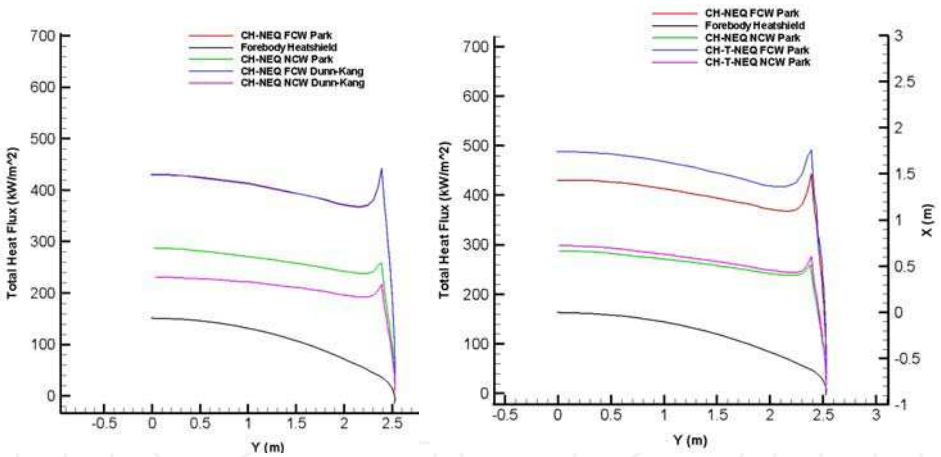

Fig. 24. Effects of chemical kinetics (left side) and of vibrational relaxation (right side) on capsule forebody total heat flux at α= 0 deg , M_∞=19 and H_∞=57 km for T_w=300 K

As far as effect of chemical kinetics is concerned, Fig. 24 shows that in the case of a FCW a large part of $\dot{q}_c$ is due to the energy released by the recombination of atoms so that the influence of chemical kinetics is small. On the contrary the differences in the heat flux profile, as evaluated for NCW, underline that the role of reaction rate may be very important in order to assess vehicle aerodynamic heating. Therefore, we can conclude that the chemical model is negligible for a catalytic wall and is significant in the non-catalytic case. Of course the latter conclusion is expected depending on freestream conditions. For instance, at high altitude the shock layer has not dissociated since pressure and density are low. Therefore, the number of particle collisions is low so that the chemical reactions are not significantly activated (e.g., the flow is nearly frozen): there is not much energy involved in dissociation. Most of the energy is in translational modes. As flying altitude decreases the

density suddenly increases and the chemical reactions are activated. At very low altitude, the shock layer is so dense that the BL is close to equilibrium (e.g., atoms recombine in the BL before they have a chance to strike the wall). Hence, the BL is heated and there is more potential for heat transfer by conduction (i.e., reactions rate comeback to have a little effect). Figure 24 also displays the effect of vibrational relaxation on the wall heat flux. As shown, the heat flux profile in the case of FCW conditions depends on vibrational relaxation more than in the case of NCW (Viviani et al., 2007).

In order to illustrate the magnitude of the effects of catalytic activity on TPS, Fig. 25 shows the comparison of the heat flux along the forebody centreline at wall radiative equilibrium conditions, between the cases of FCW, PCW and NCW, in the case of lifting re-entry (3D computations). As one can see, the overheating caused by the catalytic action is potentially very large compared with the case of NCW. In particular, the largest difference occurs at the sphere-cone junction (corner fillet) where large changes in the flow gradients along the surface occur. Therefore, the corner radius is the dominant geometric feature for the convective heating (instead of heat shield radius of curvature), and it is confirmed that significant reduction in convective heat flux occurs if the thermal shield is built with a non-catalytic TPM.

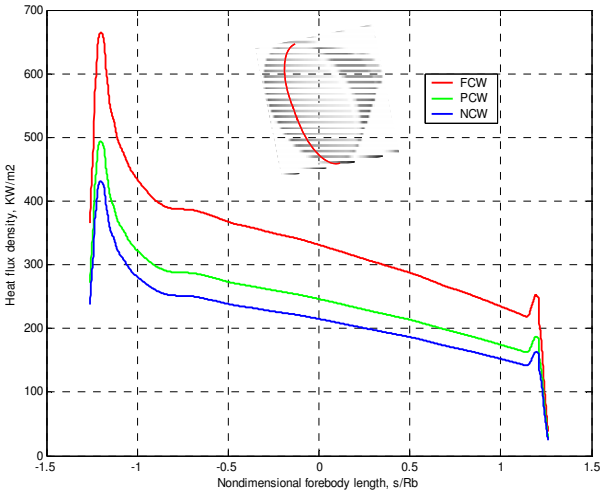

Fig. 25. Heat flux on the forebody OML. Nondimensional surface distance measured from centerline. Lifting trajectory. Vehicle trimmed at α=20 deg

10. Conclusions

Real gas effects on the design of a Crew Return Vehicle for the International Space Station have been taken into account. CFD analysis has been performed to simulate the re-entry of an Apollo-shaped capsule in order to determine the effect of thermal and chemical non-equilibrium on flowfield past the vehicle. Numerical results confirm that high temperature air conditions strongly affects both the aerodynamics and the aerothermodynamics of capsule. In particular, a comparison is made between CFD computations for perfect gas and reacting gas mixture, in order to bring into evidence the effects of finite rate chemistry, the

role of reaction mechanism with the related chemical kinetics and, finally, the influence of wall catalyticity. Model simplification is also investigated by considering a restricted set of predominant chemical reactions such as those of the Zeldovich model. Results comparisons for CRV aerodynamics confirm the strong effect of the real gas behavior on the capsule static stability. In particular, aerodynamic coefficients obtained with the Zeldovich model are within 1% of that of a solution with complete reaction mechanism, but the simulation speed up efficiency is of about 40 %. Therefore, the gain in terms of solution speed up is very high if compared with the loss in accuracy of 1% only. Anyway, in the framework of vehicle aerodynamics, the CPU speed up depends on the accuracy expected in vehicle pitching moment assessment thus confirming that the CMy is one of the most critical vehicle design parameters.

On the contrary as far as vehicle aerothermodynamic is concerned a reliable heat flux assessment over vehicle surface demands flowfield computations with a full reaction mechanism as wall catalyticity plays a significant role in the assessment of vehicle aeroheating.

Finally, the work underlines that the exact prediction of the heat transfer and chemical environment is crucial for the design of the vehicle TPS. In fact, the possibility of reducing the heat loads on the surface of space vehicles has been highlighted.

11. References

Anderson, J. D. (1989). *Hypersonic and High Temperature Gas Dynamics*, McGraw-Hill Book Company, ISBN 0-07-001671-2, New York.

Anderson, J. D. (1995). *Computational Fluid Dynamics: The Basics with Applications*, McGraw-Hill Book Company, ISBN 0-07-001685-2, New York.

Anderson, L. A. (1973). Effects of Surface Catalytic Activity on Stagnation Heat Transfer Rates. *AIAA Journal,* Vol. 11, No.5, page numbers (649-656), doi: 10.2514/3.6806.

Bertin, J. J. (1994). *Hypersonic Aerothermodynamics,* AIAA Education series, ISBN 1-56347-036-5, Washington.

Crowder R. S.; Moote J. D., (1969). Apollo Entry Aerodynamics. *Journal of Spacecraft and Rockets*, Vol. 6, No. 3, page numbers (302-307), doi: 10.2514/3.29589.

Gnoffo, P. A.; Weilmuenster K. J.; Hamilton, H. H.; Olynick, D. R.; Venkatapathy, E. (1999). Computational Aerothermodynamic Design Issues for Hypersonic Vehicles. *Journal of Spacecraft and Rockets*, Vo. 36, No. 1, page numbers (21-43). doi: 10.2514/2.3430.

Gnoffo, P. A.; Gupta, R. N.; Shinn, J. (1989). Conservation Equations and Physical Models for Hypersonic Air Flows in Thermal and Chemical Non-equilibrium. *NASA TP 2867*.

Hassan, B.; Candler, G. V.; Olynick, D. (1993). Thermo-Chemical Non-equilibrium Effects on the Aerothermodynamics of Aerobraking Vehicles. *Journal of Spacecraft and Rockets,* Vol. 30, No. 6, page numbers (647-655). doi: 10.2514/3.26369.

Lees, L., (1956). Laminar Heat Transfer over Blunt-Nosed Bodies at Hypersonic Flight Speeds", *Jet Propulsion,* Vol. 26, page numbers (259-269).

Muylaert, J.; Walpot, L.; Wennemann, D. (1999). A Review of European Code-Validation studies in High-Enthalpy Flow. *Philosophical Transactions. The Royal Society. London*. A 357, page numbers (2249-2278).

Olynick, D. (1998). Trajectory-Based Thermal Protection System Sizing for an X-33 Winged Vehicle Concept. *Journal of Spacecraft and Rockets*, Vol. 35, No. 3, page numbers (249-257). doi: 10.2514/2.3338.

Park, C.; Lee Seung-Ho. (1993) Validation of Multi-Temperature Nozzle Flow Code Noznt. *Proceedings of the 28th AIAA Thermophysics Conferences,* Orlando (FL), USA. paper AIAA-93-2862.

Park, C.; Yoont S. (1992). Calculation of Real-Gas Effects on Blunt body Trim Angles. *AIAA Journal*, Vol. 30, No. 4, page numbers (1146-1146). doi: 10.2514/3.48931.

Pezzella, G.; Battista, F.; Schettino, A.; Marini, M.; De Matteis, P. (2007). Hypersonic Aerothermal Environment Preliminary Definition of the CIRA FTB-X Re-entry Vehicle. *Proceedings of the West-East High Speed Flow Field Conferences*; Moscow, RUSSIA. Nov. (19-22).

Pezzella, G.; Votta, R. (2009). Finite Rate Chemistry Effects on the High Altitude Aerodynamics of an Apollo-Shaped Reentry Capsule", *16th AIAA/DLR/DGLR International Space Planes and Hypersonic Systems and Technologies Conference*, Bremen, Germany, Oct. 19-22. AIAA-2009-7306.

Prabhu, D. K. (2004). System Design Constraints-Trajectory Aerothermal Environments. *RTO AVT/VKI Lecture Series in Critical Technologies for Hypersonic Vehicle Development*. Rhode St. Genèse, Belgium. May (10-14).

Sarma, G. S. R. (1995). Aerothermochemistry for Hypersonic Technology. *VKI Lecture series 1995-04*. Rhode St. Genèse, Belgium.

Scott, C. D. (1987). The Effects of Thermochemistry, Non-equilibrium, and Surface Catalysis in the Design of Hypersonic Vehicles. *1th Joint Europe-US Short Course on Hypersonic. GAMNI-SMAI*. Paris, France Dec. (7-11).

Viviani, A.; Pezzella, G.; Cinquegrana, D. (2006). Aerothermodynamic Analysis of an Apollo-like Re-entry Vehicle. *Proceedings of the 14th AIAA/AHI Space Planes and Hypersonic Systems and Technologies Conferences*. 6-9 November, Canberra (AU); paper AIAA-2006-8082.

Viviani, A.; Pezzella, G.; Borrelli, S. (2008). Effect of Finite Rate Chemical Models on the Aerothermodynamics of Re-entry Capsules. *Proceedings of the 15th AIAA Space Planes and Hypersonic Systems and Technologies Conferences*. 28 April-1 May, Dayton (OH); paper AIAA-2008-2668.

Viviani, A.; Pezzella, G. (2007). Catalytic Effects on Non-Equilibrium Aerothermodynamics of a Re-entry Vehicle. *Proceedings of the 45th AIAA Aerospace Sciences Meeting and Exhibit*. 8-11 January, Reno, NE (USA); paper AIAA-2007-1211.

Viviani, A., Pezzella, G. (2007). Influence of Surface Catalyticity on Re-entry Aerothermodynamics and Heat Shield. *Proceedings of the 39th AIAA Thermophysics Conference*. 25-28 June, Miami, FL (USA); paper AIAA-2007-4047.

Viviani, A., Pezzella G. (2010). Computational Flowfield Analysis over a Blunt-Body Reentry Vehicle. *Journal of Spacecraft and Rockets*. Vol.47, No. 2, page numbers (258-270). ISSN 0022-4650. doi: 0.2514/1.40876.

Walpot, L. (2001). Numerical Analysis of the ARD Capsule in S4 Wind Tunnel. *ESA SP.487*.

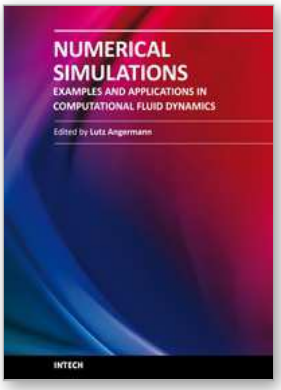

Numerical Simulations - Examples and Applications in Computational Fluid Dynamics

Edited by Prof. Lutz Angermann

ISBN 978-953-307-153-4
Hard cover, 440 pages
Publisher InTech
Published online 30, November, 2010
Published in print edition November, 2010

This book will interest researchers, scientists, engineers and graduate students in many disciplines, who make use of mathematical modeling and computer simulation. Although it represents only a small sample of the research activity on numerical simulations, the book will certainly serve as a valuable tool for researchers interested in getting involved in this multidisciplinary ï¬eld. It will be useful to encourage further experimental and theoretical researches in the above mentioned areas of numerical simulation.

How to reference

In order to correctly reference this scholarly work, feel free to copy and paste the following:

Antonio Viviani and Giuseppe Pezzella (2010). Computational Flowfield Analysis of a Planetary Entry Vehicle, Numerical Simulations - Examples and Applications in Computational Fluid Dynamics, Prof. Lutz Angermann (Ed.), ISBN: 978-953-307-153-4, InTech, Available from: http://www.intechopen.com/books/numerical-simulations-examples-and-applications-in-computational-fluid-dynamics/computational-flowfield-analysis-of-a-planetary-entry-vehicle

INTECH
open science | open minds

InTech Europe
University Campus STeP Ri
Slavka Krautzeka 83/A
51000 Rijeka, Croatia
Phone: +385 (51) 770 447
Fax: +385 (51) 686 166
www.intechopen.com

InTech China
Unit 405, Office Block, Hotel Equatorial Shanghai
No.65, Yan An Road (West), Shanghai, 200040, China
中国上海市延安西路65号上海国际贵都大饭店办公楼405单元
Phone: +86-21-62489820
Fax: +86-21-62489821